

UCLA

UCLA Previously Published Works

Title

Foxp1 suppresses cortical angiogenesis and attenuates HIF-1alpha signaling to promote neural progenitor cell maintenance.

Permalink

<https://escholarship.org/uc/item/9p80t2c4>

Journal

EMBO Reports, 25(5)

Authors

Buth, Jessie

Dyevich, Catherine

Rubin, Alexandra

et al.

Publication Date

2024-05-01

DOI

10.1038/s44319-024-00131-8

Peer reviewed

Foxp1 suppresses cortical angiogenesis and attenuates HIF-1 α signaling to promote neural progenitor cell maintenance

Jessie E Buth^{1,5}, Catherine E Dyevech^{2,5}, Alexandra Rubin², Chengbing Wang^{ID 2}, Lei Gao^{ID 3}, Tessa Marks³, Michael RM Harrison⁴, Jennifer H Kong^{ID 3}, M Elizabeth Ross^{ID 2}, Bennett G Novitch^{ID 1,6} & Caroline Alayne Pearson^{ID 2,6}✉

Abstract

Neural progenitor cells within the cerebral cortex undergo a characteristic switch between symmetric self-renewing cell divisions early in development and asymmetric neurogenic divisions later. Yet, the mechanisms controlling this transition remain unclear. Previous work has shown that early but not late neural progenitor cells (NPCs) endogenously express the autism-linked transcription factor Foxp1, and both loss and gain of Foxp1 function can alter NPC activity and fate choices. Here, we show that premature loss of Foxp1 upregulates transcriptional programs regulating angiogenesis, glycolysis, and cellular responses to hypoxia. These changes coincide with a premature destabilization of HIF-1 α , an elevation in HIF-1 α target genes, including Vegfa in NPCs, and precocious vascular network development. In vitro experiments demonstrate that stabilization of HIF-1 α in Foxp1-deficient NPCs rescues the premature differentiation phenotype and restores NPC maintenance. Our data indicate that the endogenous decline in Foxp1 expression activates the HIF-1 α transcriptional program leading to changes in the tissue environment adjacent to NPCs, which, in turn, might alter their self-renewal and neurogenic capacities.

Keywords Corticogenesis; Angiogenesis; HIF-1 Signaling; Autism; Neurodevelopment

Subject Categories Development; Neuroscience; Vascular Biology & Angiogenesis

<https://doi.org/10.1038/s44319-024-00131-8>

Received 5 June 2023; Revised 16 March 2024;

Accepted 22 March 2024

Published online: 10 April 2024

Introduction

The temporal specification of neuronal subtypes in the mammalian cortex arises through progressive changes in the transcriptional

states of cortical progenitors termed radial glia (RG) (Desai and McConnell, 2000; Shen et al, 2006). Early in development, RG undergo symmetric self-renewing cell divisions to expand the progenitor pool. Early RG (~embryonic day E12–13 in mouse) have the potential to generate all classes of excitatory glutamatergic neurons and glia (Beattie and Hippenmeyer, 2017). Late RG (~E13.5–15.5 in mice) generate basal progenitors, including intermediate progenitors and basal radial glia that, in turn, amplify the generation of later-born excitatory neurons which make up the upper layers of the cortex (Taverna et al, 2014). The precise timing of the switch from multipotent RG to more restricted RG is integral to the layered organization of the cortex and orderly assembly of circuits.

We previously demonstrated that early RG highly express the autism-linked transcription factor Foxp1, which promotes symmetric cell divisions and self-renewal, and sustains the potential to generate both early-born deep-layer neurons and later-born upper-layer neurons (Pearson et al, 2020). The endogenous down-regulation of Foxp1 in late RG at mid-neurogenic stages is required to transition to asymmetric neurogenic divisions. Conditional removal of Foxp1 function from early RG resulted in a premature transition to intermediate progenitor generation and neuronal differentiation, resulting in a reduction of early-born deep-layer neurons and a concomitant increase in upper-layer neurons (Pearson et al, 2020). However, the mechanisms through which Foxp1 promotes early RG character were unclear.

Recent single-cell RNA-Seq studies have shown that RG become increasingly responsive to extrinsic signals in the embryonic environment as development proceeds, particularly metabolic substrates made available through the developing vascular network (Telley et al, 2019; Dong et al, 2022). The switch of RG from symmetric self-renewing cell divisions to asymmetric neurogenic divisions has been associated with the relief from hypoxia as the vascular network forms and changes in RG glycolytic activity (Lange et al, 2016; Komabayashi-Suzuki et al, 2019).

Here, we show that early loss of Foxp1 in RG leads to transcriptional changes in genes associated with angiogenesis,

¹Department of Neurobiology, Eli and Edythe Broad Center of Regenerative Medicine and Stem Cell Research, Intellectual and Developmental Disabilities Research Center, David Geffen School of Medicine at UCLA, Los Angeles, CA 90095, USA. ²Feil Family Brain and Mind Research Institute and Center for Neurogenetics, Weill Cornell Medicine, New York, NY 10021, USA. ³Department of Biochemistry, University of Washington, Seattle, WA 98195, USA. ⁴Cardiovascular Research Institute, Weill Cornell Medicine, New York, NY 10021, USA. ⁵These authors contributed equally: Jessie E Buth, Catherine E Dyevech. ⁶These authors contributed equally as senior authors: Bennett G Novitch, Caroline Alayne Pearson. ✉E-mail: cap4010@med.cornell.edu

Hypoxia Inducible Factor 1 alpha (HIF-1 α) signaling, and glycolysis. In situ hybridization (ISH) and immunohistochemical (IHC) analyses demonstrated that many of the deregulated genes, including the HIF-1 α targets *Vegfa*, *Slc2a1* (encodes glucose transporter 1, Glut1), and *Ldha* (encodes Lactate dehydrogenase A), are expressed by early RG. We further observed that *Vegfa* transcript and protein are endogenously upregulated in RG as Foxp1 levels decline, and these changes coincide with the onset of angiogenesis. Moreover, the deletion of Foxp1 from early cortical progenitors resulted in early destabilization of HIF-1 α protein, upregulation of HIF-1 α targets, including Glut1, *Ldha*, and *Vegfa*, and accelerated development of the cortical vasculature. Finally, our in vitro studies demonstrate that HIF-1 α stabilization is sufficient to rescue the premature differentiation of Foxp1-deficient neural progenitor cells (NPCs). These findings reveal that Foxp1 attenuates the HIF-1 α signaling pathway, suppressing angiogenesis and prolonging conditions that sustain early RG character.

Results and discussion

Early loss of Foxp1 in radial glia upregulates genes associated with neuronal differentiation, angiogenesis, HIF-1 signaling, and glycolysis

To examine the role of Foxp1 directing the transition from self-renewal to neurogenic divisions, we dissected samples of the lateral cortex (within the presumptive somatosensory cortex) from embryonic day (E)12.5 control (*Emx1^{Cre}* negative littermates) and *Foxp1^{fl/fl}; Emx1^{Cre/+}* (termed *Foxp1^{CKO}*) mutant embryos and performed bulk RNA-Seq analysis (Figs. 1A and EV1A–C). We previously demonstrated that Cre recombination occurs at E10.5, and significant Foxp1 protein loss occurs at E11.5 (Pearson et al, 2020). Of the 514 significantly misregulated genes, 307 were upregulated (\log_2 fold change >0.5), and 80 were downregulated (\log_2 fold change <–0.5), consistent with the reported role of Foxp1 as a transcriptional repressor in other tissues (Zhang et al, 2010) (Fig. EV1A and Tables EV1–EV2). The main human disease categories associated with these upregulated genes included schizophrenia, autism, intellectual disorders, neurodevelopmental disorders, glycogen storage disorders, and seizures (Fig. EV1B). Gene ontology analyses showed that terms associated with DNA replication, cell cycle/mitosis, and RNA metabolism were under-represented in the absence of Foxp1 (Fig. 1B). Concordantly, subcellular compartments associated with the top downregulated genes included the cyclin E1-CDK2 complex, the replication fork, and the mitochondrion (Table EV3). Without Foxp1, biological processes such as nervous system development, neuron differentiation, and cell-cell signaling were overrepresented (Fig. 1B). In addition, among the most overrepresented processes and pathways in *Foxp1^{CKO}* cortices were responses to cell-cell signaling, regulation of blood circulation, glycolysis/gluconeogenesis, and HIF-1 signaling (Fig. 1B). Subcellular compartments associated with the upregulated genes include the 6-phosphofructokinase complex, glucose transporter complex, and synapses (Table EV4).

Consistent with these findings, we found that many essential genes involved in glycolysis, HIF-1 signaling, and angiogenesis were upregulated in the absence of Foxp1, including *Vegfa*, *Ldha*, and *Slc2a1* (Fig. 1C). Thus, early loss of Foxp1 in RG leads to

transcriptional increases in genes associated with differentiation, angiogenesis, and increased dependence on metabolites such as oxygen and glucose.

The endogenous downregulation of Foxp1 coincides with the elaboration of the cortical vasculature

Given the increased expression of genes connected to processes such as blood circulation in Foxp1 mutants, we asked whether Foxp1 downregulation during normal cortical development coincided with changes in cortical vasculature. IHC analysis of Foxp1 protein levels in RG and the presence of Isolectin IB4⁺ blood vessels, followed by surface rendering of the blood vessels, enabled us to distinguish periventricular plexus (PVP) vessels from those originating from the perineural vascular plexus (PNVP). Our analyses confirmed that there are few PVP vessels at E12.5 when Foxp1 levels are highest (Fig. 1D,G,H). As previously reported (Vasudevan et al, 2008), the cortex is perfused ventrodorsally (Fig. 1D). Foxp1 downregulation at E13.5 coincides with the onset of angiogenesis in the cortex, i.e., an increased number of vessels per section, followed by an increase in PVP vessel volume at E14.5 (Fig. 1E–I). At these time points, we observed a significant increase in Tbr2⁺ IPs and cortical plate thickness as TUJ1⁺ neurons were generated (Figs. 1E,F,J,K and EV1D–F).

Foxp1 attenuates the HIF-1 α signaling response in radial glia

Previous reports demonstrated that HIF-1 α expression is destabilized between E11.5 and E12.5 (Lange et al, 2016). Using IHC, we analyzed HIF-1 α expression and found it is expressed in Nestin⁺ RG at E11.5 when Foxp1 expression is low (Fig. 2A–D). By the next day (E12.5), HIF-1 α is downregulated in the cortex as Foxp1 expression increases (Fig. 2E–H). HIF-1 α expression was detected in Nestin⁺ RG at low levels in the dorsal-most lateral cortex and higher levels in the medial cortex (Fig. 2I,J). This pattern is consistent with the ventral to dorsal vascularization of the cortex. In *Foxp1^{CKO}* cortices at E12.5, while HIF-1 α expression in the dorsolateral cortex remained low/absent, there was a significant decrease in HIF-1 α staining in the medial cortex (Fig. 2K–N).

Next, we sought to determine whether RG express key HIF-1 α targets at E12.5. From our RNA-Seq dataset, we selected HIF-1 α targets involved in glycolysis and analyzed expression by ISH. Several glycolysis genes are specifically expressed in the VZ, including *Slc2a1*, *Ldha*, *Aldoa*, *Pfk1*, *Pfkfb3*, *Pdk1*, and *Slc16a4* (Fig. EV2A–G). Western blot analyses of E11.5, E12.5, and E13.5 wild-type cortex lysates demonstrate HIF-1 α protein levels decrease while Glut1 levels increase (Fig. EV2H–J). *Ldha* levels decrease between E11.5 and E12.5 but remain stable between E12.5 and E13.5 (Fig. EV2H,K). *Vegfa* levels similarly decrease between E11.5 and E12.5, though slightly increase between E12.5 and E13.5 (Fig. EV2H,L). A caveat to this analysis is that protein lysates include RG and other cell types in the cortex at each stage, including endothelial cells. Thus, we performed IHC with each antibody and Nestin to better assess protein abundance in RG.

IHC analysis showed that Glut1 protein is expressed in Nestin⁺ RG with pronounced accumulation at their apical end feet at E12.5 and E13.5 (Fig. EV2M,O,Q–T). Additional Nestin co-staining analysis confirmed *Ldha* expression in RG (Fig. EV2N,P,U–X). Thus, several HIF-1 α targets, including Glut1 and *Ldha*, persist in RG, while HIF-1 α expression itself is downregulated between E11.5 and E12.5.

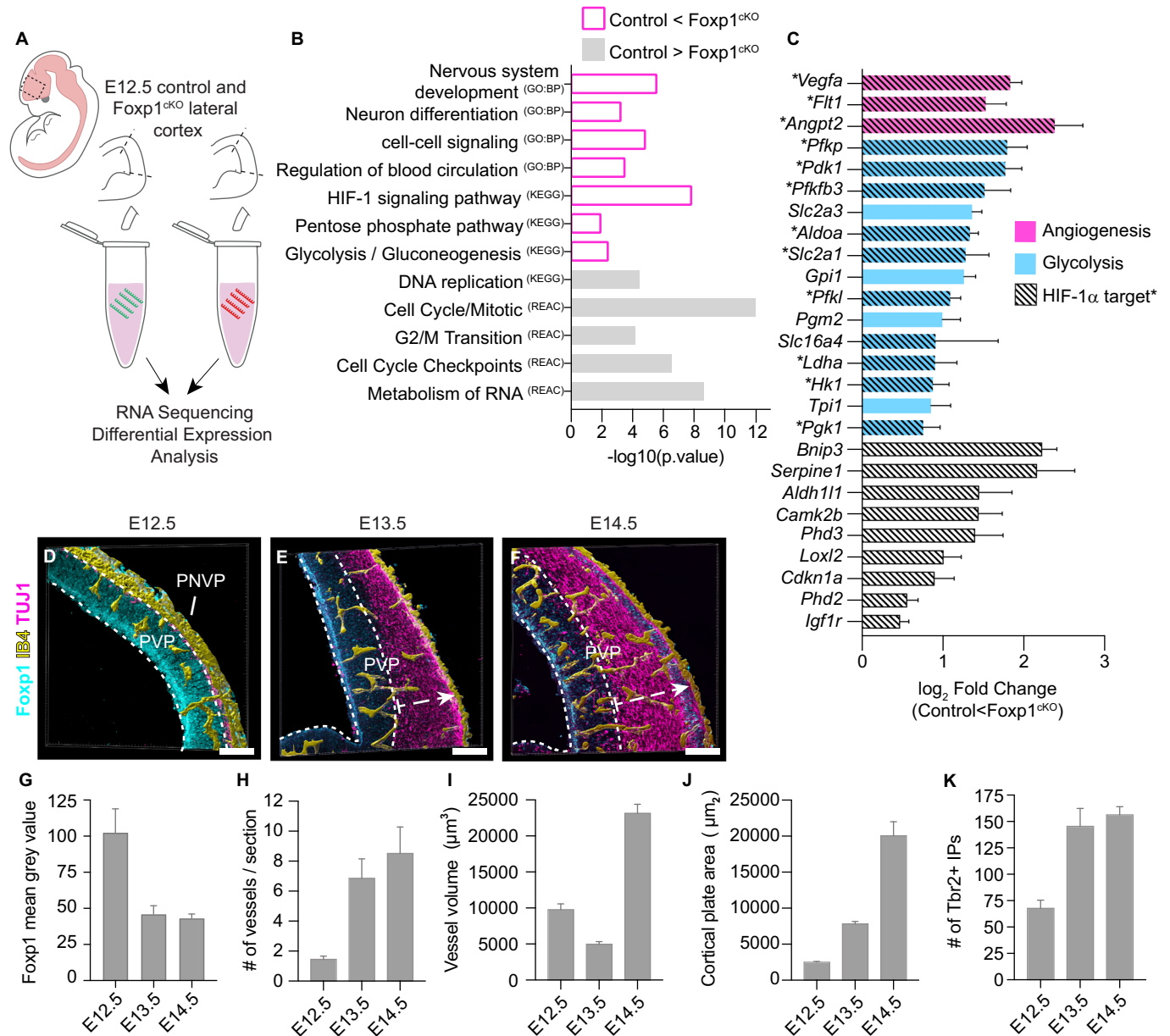
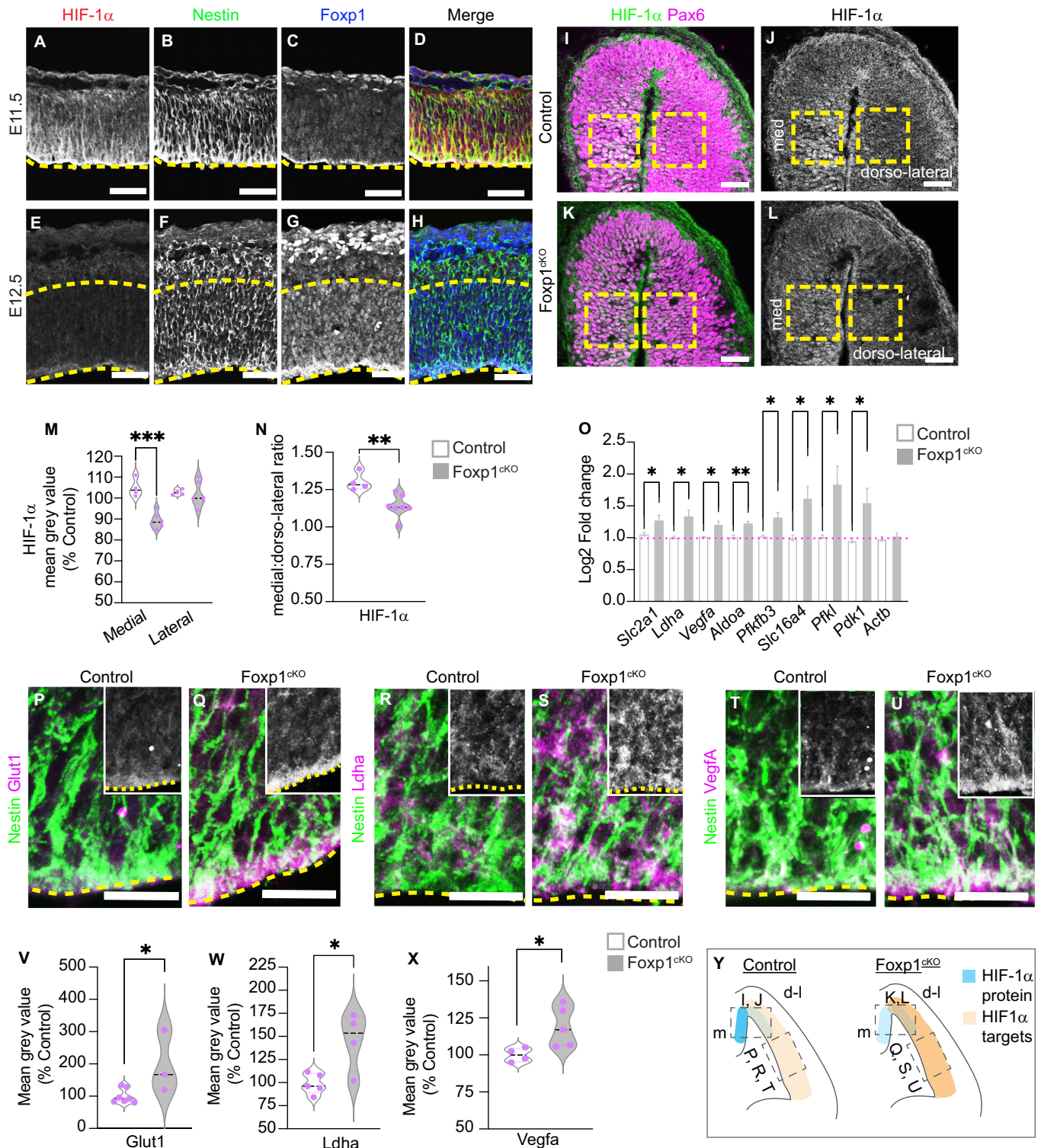


Figure 1. Processes regulating angiogenesis, HIF-1 α signaling, and glycolysis are upregulated upon conditional removal of Foxp1.

(A) RNA collected from E12.5 control and Foxp1^{CKO} cortices. (B) Gene ontology terms associated with significantly misregulated genes in the Foxp1^{CKO} cortex at E12.5. GO terms: BP, biological process; KEGG, pathways, REAC, reactome pathway. (C) Significantly misregulated genes associated with angiogenesis (magenta), glycolysis (blue), and HIF-1 α signaling (white/hashed lines) in Foxp1^{CKO}s at E12.5. * and bars with hashed lines are also HIF-1 α targets. (D-F) 3D surface rendering of IB4⁺ blood vessels in the cortex from E12.5 to E14.5 with Foxp1 and TUJ1 expression. White dashed arrows delineate cortical plate. (G-J) Foxp1 intensity, periventricular plexus vessel (PVP) number, volume, and cortical plate area in the lateral cortex at E12.5-E14.5. (K) Number of Tbr2⁺ progenitors (per 200 μ m²) in wild-type cortex at E12.5-E14.5. Scale bars 100 μ m. Data information: Statistical significance determined by ANOVA (B, C). $N = 4$ controls, 2 mutants (B, C). $N = 5$ (G), 4 (H), 3-4 (I), 3-4 (J), 3-4 (K) embryos/time point. All data represented as mean \pm SEM. Source data are available online for this figure.

To explore the connection between Foxp1 and HIF-1 α signaling, we next confirmed by qPCR that several key HIF-1 α targets are upregulated at E12.5 in the absence of Foxp1, including *Slc2a1*, *Ldha*, *Aldoa*, *Pfkf1*, *Pfkfb3*, *Pdk1*, and *Slc16a4* (Fig. 2O). We subsequently analyzed Glut1 and *Ldha* protein levels and found that both proteins were significantly increased in Nestin⁺ RG lacking Foxp1 function (Fig. 2P-S,V,W). Thus, while HIF-1 α targets are elevated in the absence of Foxp1, HIF-1 α protein

becomes reduced. These data suggest that Foxp1 typically acts to stabilize HIF-1 α protein yet attenuate its signaling functions. These opposing actions of Foxp1 on HIF-1 α are not without precedent, as previous studies have demonstrated that prolonged hypoxia can trigger negative feedback loops where HIF-1 α protein becomes unstable or is expressed in a pulsatile manner (Nguyen et al, 2013; Bagnall et al, 2014). Likewise, some studies have shown that the Cdk2/cyclin E cell cycle regulators can inhibit HIF-1 α protein levels



while increasing HIF1 transcriptional activity (Sengupta et al, 2011; Hubbi et al, 2014). This latter observation may be relevant as our RNA-seq analysis singled out the Cdk2/cyclin E complex as among the most changed cellular compartments in Fo xp1 mutant cortices (Tables EV2 and 3).

Vegfa upregulation in Fo xp1-deficient radial glia

The HIF-1α target gene Vegfa is a critical mediator of cortical angiogenesis and among the most upregulated genes in our RNA-seq analysis (Figs. 1C and EV1A). RNAScope analysis of Vegfa and

Figure 2. HIF-1 α expression is reduced, and HIF-1 α targets are upregulated in RG in the absence of Foxp1.

(A–H) IHC analysis of HIF-1 α and Foxp1 in Nestin⁺ RG at E11.5 and E12.5 wild-type cortex. (I–L) IHC analysis of Pax6 and HIF-1 α expression in the medial and dorsolateral cortex at E12.5 in control and Foxp1^{CKO} mutants. Boxed areas indicate regions quantified in (M) and (N). (M, N) HIF-1 α mean gray value (percent control) and medial to dorsal ratio in control and Foxp1^{CKO} mutant cortex at E12.5. (O) Quantification of mRNA fold enrichment (normalized to *Actb*) for *Slc2a1*, *Ldha*, *Vegfa*, *Aldoa*, *Pfkfb3*, *Slc16a4*, *Pfkl*, *Pdk1*, and *Actb* in control and Foxp1^{CKO} by qPCR in the lateral cortex at E12.5. (P–U) IHC for Glut1, *Ldha*, *Vegfa*, and Nestin in control and Foxp1^{CKO} mutants in the VZ of the cortex at E12.5. The inset is Glut1/*Ldha*/*Vegfa* only. (V) Glut1 mean gray value (percent control) in control and Foxp1^{CKO} mutant Nestin⁺ RG at E12.5. (W) *Ldha* mean gray value (percent control) in control and Foxp1^{CKO} cortex at E12.5. (X) *Vegfa* mean gray value (percent control) in control and Foxp1^{CKO} cortex at E12.5. (Y) Summary of HIF-1 α and target gene expression in control and Foxp1^{CKO} cortex at E12.5. Dashed lines demarcate the ventricular zone. Scale bars 50 μ m (A–L), 20 μ m (P–U). Data information: $p = 0.0003$ and 0.0055 , respectively, Student's t-test. $N = 7$ control, 6 mutants (M, N). $N = 3$ control, 3 mutants (3 litters). p values = 0.039 (*Slc2a1*), 0.0256 (*Ldha*), 0.013 (*Vegfa*), 0.0073 (*Aldoa*), 0.0177 (*Pfkfb3*), 0.0152 (*Slc16a4*), 0.0183 (*Pfkl*), 0.0392 (*Pdk1*). Student's t-test (O). $p = 0.0262$, Student's t-test. $N = 7$ control, 3 mutants (V). $p = 0.0169$, Student's t-test. $N = 5$ control, 4 mutants (W). $p = 0.0328$, Student's t-test. $N = 4$ control, 5 mutants (X). All data represented as mean \pm SEM. Source data are available online for this figure.

Foxp1 expression demonstrated the upregulation of *Vegfa* expression in the VZ at E13.5 and E14.5, whereas *Foxp1* is downregulated. *Vegfa* and *Foxp1* are also both expressed in the cortical plate (Fig. EV3A–D). IHC analysis of *Vegfa* protein in wild-type tissue between E12.5 and E14.5 confirmed its upregulation in Nestin⁺ RG from E13.5 onwards, with accumulation at the apical surface of the VZ (Fig. EV3E–K). Co-staining analysis of *Vegfa* protein with Nestin and Foxp1 further showed that E12.5 Nestin⁺ RG express high levels of Foxp1 and low levels of *Vegfa* (Fig. EV3L–O) while E14.5 Nestin⁺ RG express low levels of Foxp1 and increased levels of *Vegfa* (Fig. EV3P–S).

To determine whether *Vegfa* levels were affected by the loss of Foxp1 in RG, we compared the intensity of *Vegfa* expression in Nestin⁺ RG in control and Foxp1^{CKO} cortex at E12.5 by IHC. This analysis confirmed that *Vegfa* is increased in Foxp1^{CKO} RG (Fig. 2T,U,X). The transcriptional increase in *Vegfa* expression was demonstrated by qPCR analysis in the control and Foxp1^{CKO} cortex at E12.5 (Fig. 2O). IHC analysis of *Vegfa* expression levels in the cortical plate showed no significant difference between control and Foxp1^{CKO} cortices (Fig. EV3T–V). Thus, the upregulation of *Vegfa* within RG appears to coincide with the endogenous downregulation of Foxp1 and increased angiogenesis in the cortex. Premature loss of Foxp1 leads to an increase in *Vegfa* expression in RG (Fig. 2Y).

Deletion of Foxp1 accelerates the development of the cortical vasculature

Given the upregulation of *Vegfa* and the downregulation of HIF-1 α in the absence of Foxp1, we asked whether the loss of Foxp1 impacted cortical angiogenesis. Initially, we examined how this manipulation influenced the ventrodorsal expansion of the PVP network within the E12.5 cortex using surface-rendered projections of IB4⁺ vessels in 50- μ m-thick cryosections of control and Foxp1^{CKO} embryos. At E12.5, comparable numbers of vessels were present in the mid and ventrolateral cortex but appeared to increase in the dorsolateral region of Foxp1^{CKO} samples (Fig. 3A–D). To quantify these differences, we divided the cortex into three areas of equal size. We counted the number of vessels in each region, which confirmed a significant increase in vessels in the dorsolateral area (Fig. 3E,F). Thus, increased *Vegfa* expression and HIF-1 α downregulation coincided with increased vasculature in the Foxp1-deficient dorsolateral cortex. While IB4 can be expressed by other cell types, including microglia in the developing brain (Cunningham et al, 2013; Penna et al, 2021), at the stages we investigated, we found that IB4 exclusively labeled CD31⁺ endothelial cells

(Appendix Fig. S1A–F). However, IB4-labeling of filopodia was more evident than CD31 and easier to visualize and quantify (Appendix Fig. S1G,H). We observed a higher density of tip cell filopodia in Foxp1^{CKO} samples at E12.5 compared to controls (Fig. 3G,H,M), which is consistent with previous observations that increased *Vegfa* signaling can induce the formation of endothelial tip cell filopodia (Gerhardt et al, 2003; Haigh et al, 2003).

We next analyzed the cortical vasculature a day later at E13.5. At this stage in control embryos, the cortex has been perfused by contiguous IB4⁺ vessels along the dorsoventral axis that have begun to form branches (Fig. 3I,K). Parallel analysis of Foxp1^{CKO} cortices showed that their blood vessels were significantly more extended and branched, and volume increased compared to controls (Fig. 3J,L,N–P). Collectively, these results demonstrate that deletion of Foxp1 results in a premature establishment of cortical vasculature in the dorsal-most lateral cortex and the development of the vascular network in a non-stereotypical fashion.

Other signals have been shown to regulate cortical angiogenesis, including lactate and Wnts (Daneman et al, 2009; Dong et al, 2022). Wnt genes were not significantly misregulated in our RNA-Seq analyses, suggesting that Foxp1 may act independently of Wnt signaling to influence angiogenesis. Foxp1 is also expressed in neurons, as is *Vegfa* (Fig. EV3A–D), raising the possibility that at later stages, loss of Foxp1 in neurons may also influence angiogenesis. The changes we have shown here in *Ldha* and other glycolysis genes in the absence of Foxp1 could reflect the increased availability of glucose in the RG microenvironment. Mouse models of maternal diabetes have shown that moderate hyperglycemia leads to premature RG differentiation (Ji et al, 2019). Thus, increases in environmental glucose could also influence the balance between RG self-renewal and differentiation (Andrews and Pearson, 2024).

HIF-1 α stabilization rescues early differentiation phenotypes in Foxp1-deficient NPCs

Given our results, we hypothesized that Foxp1 promotes RG maintenance by stabilizing HIF-1 α and attenuating the HIF-1 α signaling response to promote hypoxic conditions that favor self-renewal. To test this hypothesis, we generated cortical spheroids from control and Foxp1^{CKO} mouse embryonic stem cells (mESCs). This in vitro approach also enabled us to determine the cell-autonomous effects of Foxp1. We used two Foxp1^{CKO} mESC lines in which the genomic region encoding the Foxp1 forkhead domain required for DNA binding was deleted using CRISPR-Cas9 editing (Appendix Fig. S2). This modification caused a reduction in Foxp1 protein levels and truncated the sizes of both isoforms A and D

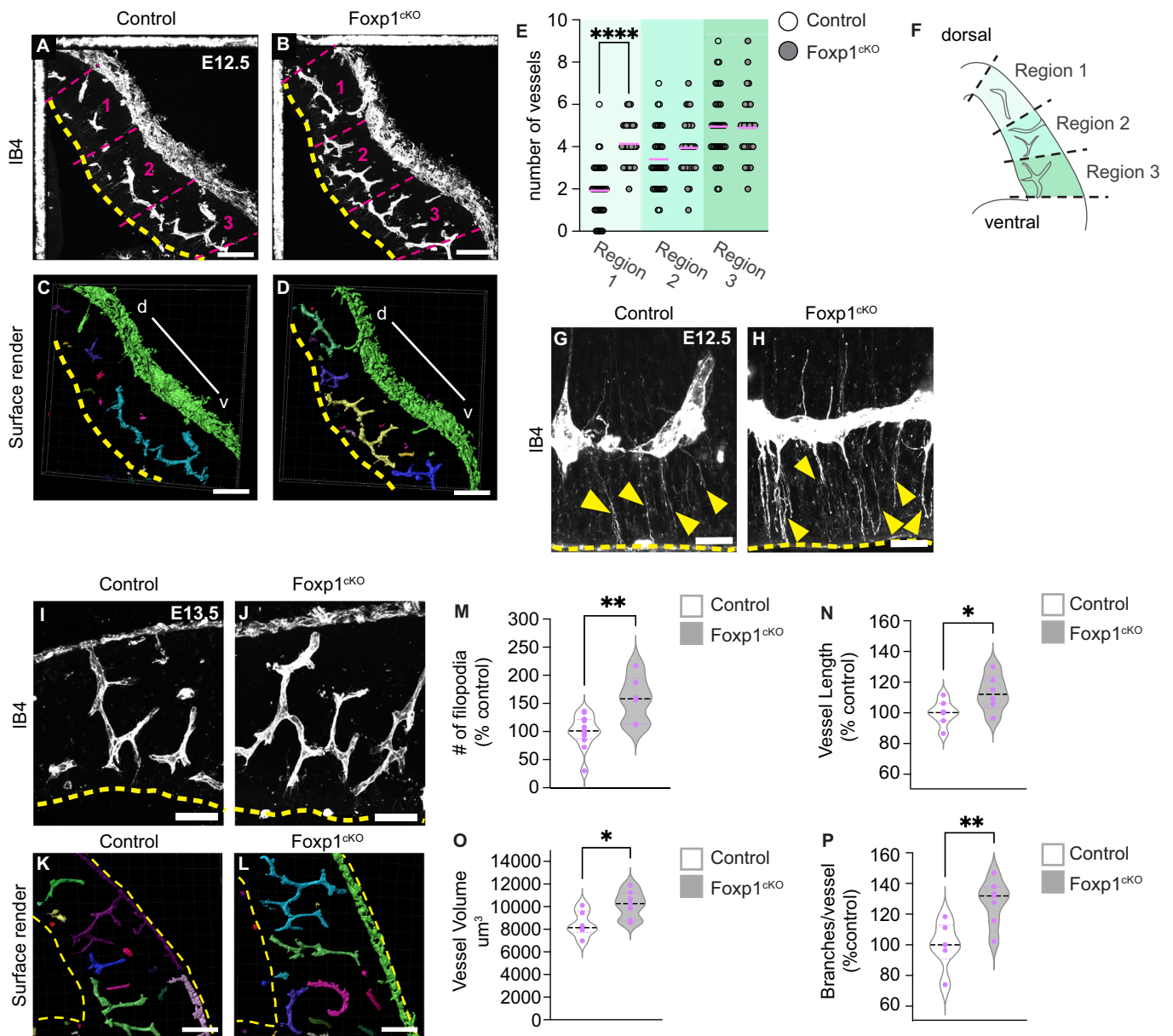
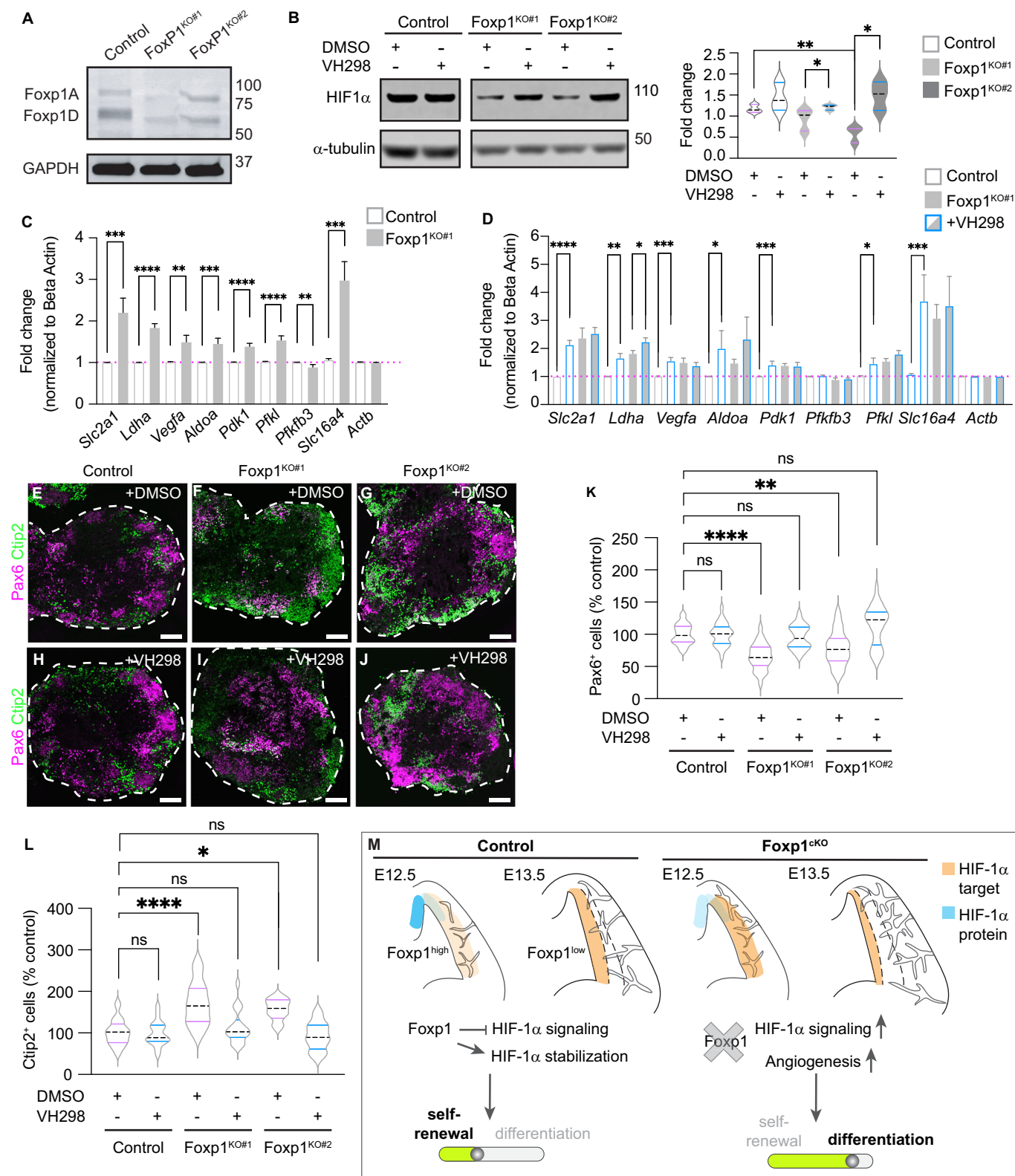


(Fig. 4A). Spheroids at day 7 in vitro (div) were mainly composed of Pax6⁺ NPCs, and very few cells expressed neuronal markers such as Tbr1 or Ctip2, with little difference seen between control and Foxp1^{ckO} samples (Fig. EV4A–F). The loss of Foxp1 protein in Pax6⁺ NPCs was confirmed by IHC (Fig. EV4H–P). By 10 div, we observed Foxp1 loss in spheroids recapitulates the in vivo phenotype. Western blot analyses showed that HIF-1α protein levels are decreased in the absence of Foxp1 (Fig. 4B). qPCR

analysis demonstrated that the expression of HIF-1α target genes is increased in Foxp1^{ckO} spheroids, except for *Pfkfb3* which was decreased in Foxp1^{ckO#1} (Figs. 4C and EV4G). In addition, we observed a significant decrease in the number of Pax6⁺ NPCs and a concomitant increase in Ctip2⁺ neurons in spheroids generated from both Foxp1^{ckO} lines (Fig. 4E–L).

To test whether the precocious differentiation phenotype seen in the Foxp1^{ckO} spheroids could be rescued by HIF-1α manipulation,



we treated spheroids at 7 div with VH298, a Von Hippel-Lindau E3 ligase inhibitor that stabilizes HIF-1 α (Frost et al, 2016). Western blot analyses confirmed the stabilization of HIF-1 α in control and Foxp1^{KO} spheroids treated with VH298, and the treatment

correlated with increased expression of HIF-1 α target genes in control spheroids (Fig. 4B,C). In Foxp1^{KO} spheroids, the transcriptional response to VH298 was markedly reduced or showed no change compared to the response in control spheroids, except for

Figure 4. HIF-1 α stabilization promotes NPC maintenance in Foxp1-deficient cortical spheroids.

(A) Western blot analysis of Foxp1 and GAPDH protein in control and Foxp1^{KO} mouse embryonic stem cells. (B) Western blot analysis and quantification of HIF-1 α protein (compared to α -tubulin) in control and Foxp1^{KO} spheroids at 10 div treated with DMSO or VH298. (C) qPCR analysis of HIF-1 α target gene expression in control and Foxp1^{KO#1} spheroids at 10 div. (D) qPCR analysis of HIF-1 α target gene expression in control and Foxp1^{KO#1} spheroids at 10 div. treated with DMSO or VH298. (E–J) IHC for Pax6⁺ NPCs and Ctip2⁺ neurons in control and Foxp1^{KO} spheroids (10 div) treated with DMSO or VH298. (K) Percentage of DAPI⁺ cells that are Pax6⁺ in control and Foxp1^{KO} spheroids (10 div) treated with DMSO or VH298. (L) Percentage of DAPI⁺ cells that are Ctip2⁺ in control and Foxp1^{KO} spheroids (10 div) treated with DMSO or VH298. (M) Schematic of control and Foxp1^{KO} phenotypes. Foxp1 attenuates the HIF-1 α signaling pathway to promote RG self-renewal. In the absence of Foxp1, HIF-1 α target gene expression is upregulated, angiogenesis is perturbed, and RG precociously differentiate. Scale bars 100 μ m. Data information: $p = **0.0097, 0.00364$ (Foxp1^{KO#1}) and 0.0162 (Foxp1^{KO#2}). Student's t-test. $N = 10$ – 12 spheroids, western blots run in triplicate (B). p values = 0.0008 (*Slc2a1*), <0.0001 (*Ldha*), 0.0026 (*Vegfa*), 0.0010 (*Aldoa*), <0.0001 (*Pdk1*), <0.001 (*Pfkfb3*), 0.0061 (*Pfkfb3*, Mann-Whitney test), 0.0001 (*Slc16a4*). $N = 10$ – 12 spheroids/experiment, 3 experiments (C). p values = <0.0001 (*Slc2a1*, control), 0.0013 (*Ldha*, control), 0.0446 (*Ldha*, Foxp1^{KO#1}), 0.0002 (*Vegfa*, control), 0.0179 (*Aldoa*, control), 0.0002 (*Pdk1*, control), 0.0201 (*Pkfb3*, control), 0.0003 (*Slc16a4*, control). $N = 10$ – 12 spheroids/experiment, 3 experiments (D). One-way ANOVA, $p = >0.9999, <0.0001, 0.928, 0.0024$ and 0.1066 , respectively. $N = 10$ – 12 spheroids/experiment, 3 experiments (K). Ordinary one-way ANOVA, $p = >0.9999, <0.0001, 0.8306, 0.0196, 0.9883$. $N = 10$ – 12 spheroids/experiment, 3 experiments (L). All data represented as mean \pm SEM. Source data are available online for this figure.

Ldha in Foxp1^{KO#1} and *Pdk1* in Foxp1^{KO#2} spheroids, which exhibited significant increases (Figs. 4D and EV4Q). These effects may reflect the reduced HIF-1 α levels seen in Foxp1^{KO} spheroids compared to controls. Additional analysis of the percentage of cells that are Pax6⁺ NPCs or Ctip2⁺ neurons demonstrated a significant increase in NPCs in Foxp1^{KO} spheroids treated with VH298 and a concomitant decrease in Ctip2⁺ neurons compared to DMSO-treated Foxp1^{KO} spheroids (Fig. 4E–L). Moreover, after VH298 treatment, the proportion of Pax6⁺ NPCs and Ctip2⁺ neurons in Foxp1^{KO} spheroids was similar to DMSO-treated control spheroids. Thus, HIF-1 α stabilization appears sufficient to rescue defects in NPC maintenance and premature differentiation associated with Foxp1 deficiency.

Integrating these findings with our prior investigations into the effects of Foxp1 gain- and loss-of-function on cortical progenitor activities (Pearson et al, 2020), our studies suggest that Foxp1 shapes the transition of RG through early-to-late stages of neurogenesis by promoting a hypoxic stem cell niche microenvironment. Early on, Foxp1 suppresses the downstream effectors of HIF-1 α , such as *Vegfa*, that lead to relief from hypoxia, thus delaying angiogenesis and the transition to oxygenated conditions. This suppression promotes an environment favorable for early self-renewing cell divisions. As Foxp1 levels in RG endogenously decline, or when Foxp1 function is experimentally ablated, HIF-1 α target gene expression levels increase, and HIF-1 α is further destabilized. These effects drive the elaboration of the cortical vasculature and the switch to neurogenic divisions (Fig. 4M). These findings complement and extend previous reports demonstrating that hypoxic conditions and the suppression of vascular ingrowth repress the switch to neurogenesis (Lange et al, 2016; Komabayashi-Suzuki et al, 2019; Dong et al, 2022).

The cellular response to hypoxia activates a transcriptional cascade that drives processes that enable a transition to a normoxic environment and processes that promote cell survival and proliferation (Corrado and Fontana, 2020). Factors have been identified that selectively regulate cellular responses to hypoxia, including Runt-related (Runx) transcription factors that modulate HIF-1 α stability and transcriptional activity to regulate *Vegfa* expression during angiogenesis (Peng et al, 2008; Lee et al, 2012, 2014; Brocato et al, 2014). Therefore, cells can dissociate the proliferative effects of HIF-1 α signaling and the adaptive effects, such as glycolysis and angiogenesis. Our in vitro experiments reveal an intrinsic role for Foxp1 in promoting cell proliferation and repressing angiogenesis and glycolysis, identifying Foxp1 as a key regulator of the HIF-1 α signaling pathway in early RG.

Presently, the mechanisms driving Foxp1 downregulation in RG cells across development are unknown, though several factors could be involved. HIF-1 α has been shown to directly bind and regulate the expression of Jumonji domain-containing histone demethylases such as *Jarid1b* (*Kdm5b*), and studies have shown that the range of HIF-1 α targets is determined by cell type specific patterns of chromatin structure (Brocato et al, 2014). Recently, a related factor, *Jarid2*, was identified as a repressor of early Foxp1 in retinal progenitors (Zhang et al, 2023). Further studies are required to determine whether a similar mechanism is utilized in RG. Another regulatory mechanism may involve microRNAs, which have been shown to regulate Foxp proteins in many organ systems (Li et al, 2017). miR-9 has been demonstrated to inhibit factors that regulate *Vegfa* expression in retinal and telencephalic neurons, coupling neurogenesis and the maturation of the vasculature (Madelaine et al, 2017). Foxp1 is a target of miR-9 in a variety of contexts, including in motor neurons in the developing spinal cord (Otaegi et al, 2011; Gomez et al, 2014; Radhakrishnan and Alwin Prem Anand, 2016; Jiang et al, 2017). Potentially, a similar miR-9-dependent mechanism could be used to regulate Foxp1 and *Vegfa* expression in RG.

An increasing body of evidence has implicated blood vessel pathologies in several neurodevelopmental disorders (Baruah and Vasudevan, 2019; Ouellette and Lacoste, 2021). For example, early defects in PVP endothelial cells have been linked to the origin of autism (Azmitia et al, 2016). Further investigation is required to determine whether the mild alterations we observe in the Foxp1^{CKO} cortex can have long-term effects on brain function. Foxp1 is also expressed in endothelial cells and has been shown to promote angiogenesis in various contexts (Grundmann et al, 2013). Further dissection of the neural and endothelial contributions of Foxp1 to brain angiogenesis will be critical for understanding the role of *FOXPI* in neurodevelopmental disorders.

Methods

Mouse lines

C57BL6 wild-type (RRID: IMSR_JAX:000664), Foxp1^{fllox/fllox} (RRID: IMSR_JAX:017699), and *Emx1*^{Cre} (RRID: IMSR_RBRC01342) mice were maintained as previously described (Iwasato et al, 2004; Feng et al, 2010) following UCLA Chancellor's Animal Research Committee husbandry guidelines. All experiments were conducted

in accordance with relevant NIH guidelines and regulations, related to the Care and Use of Laboratory Animals tissue. Animal procedures were performed according to protocols approved by the Research Animal Resource Center at Weill Cornell College of Medicine. Wild-type litters were provided by the Mouse Genetics Core Facility at Memorial Sloan Kettering Cancer Center. Male and female embryos between embryonic days 11.5 and 13.5 were used in this study. Cre-negative littermates were used as controls.

Foxp1 knock out mouse embryonic stem cell line generation

The Foxp1 gene was disrupted in MM13 mouse embryonic stem cells (mESCs). To disrupt Foxp1 function, CRISPR/Cas9-mediated genome editing was used to target the forkhead domain. Using Benchling, two guides were designed targeting Exon 12 of Foxp1-201 (ENSMUST00000074346): 5'-AGATTTCGAGAATGGCCTACG-3' and 5'-TGCAAAGCTTACCTTCCACG-3'. These sequences were individually cloned into plasmid pSpCas9(BB)-2A-Puro (PX459) V2.0 (Addgene #62988) and then electroporated into the mESCs using the Lonza Nucleofector 2b Device and Cell Nucleofector Kit (Lonza #VAPH-1001). The mESCs were cultured in feeder-free 2i media (DMEM/F-12 (Gibco #11320033) and Neurobasal Medium (Gibco #21103049) (prepared at a 1:1 ratio) supplemented with N2 supplement (Gibco #17502048), B27 serum-free supplement (Gibco #17504044), penicillin/streptomycin (Gibco #15140122), glutaMAX (Gibco #35050061), bovine serum albumin (Thermo Scientific Chemicals #AAJ64248AE), 55 μ M 2-mercaptoethanol (Gibco #21985023), 3 μ M CHIR99021 (Axon #1386), 1 μ M PD 98059 (Tocris Bioscience #1213), and ESGRO recombinant mouse LIF protein (1000 units/ml, MilliporeSigma #ESG1107)]. Antibiotic selection was initiated 24 h after nucleofection in 2i media containing 1.5 μ g/ml puromycin (Fisher BioReagents #BP2956100) for ~72 h. Clones were picked individually, expanded in feeder-free 2i media, and genomic DNA was collected using QuickExtract DNA extraction solution (Lucigen, #QE09050). The region surrounding the targeted site was PCR-amplified (using the primers Forward 5'-TTTGTGAAACCTGCCTGAGGA-3' and Reverse 5'-GGTCAACAAGGTCACCTCCTT-3') to visualize a successful deletion facilitated by the guides. A loss of full-length FOXP1 protein was then verified by Western blot using a protein-specific antibody (Cell Signaling Technology, #4402T).

Mouse embryonic stem cell maintenance

MM13 mESCs were maintained in 2i mESC media on 0.1% gelatin-coated plates. DMEM/F12 (50%) and Neurobasal (50%) basal media was supplemented with 0.5% N2, 1% B27, 1% penicillin-streptomycin, 1% Glutamax, beta mercaptoethanol. Cells were fed daily, media was supplemented with 10 ng/ml human LIF, 10 μ M CHIR, 1 μ M PD98059. mESCs were routinely tested for mycoplasma.

Cortical neural progenitor cell and neuronal differentiation

Cortical neural progenitor cells and neurons were generated using the protocol established by Eiraku et al (Eiraku and Sasai, 2011). In brief, 3000 mESCs were plated per well of a 96-well U-bottomed ultra-low attachment plates. Cells were cultured in cortical differentiation media (GMEM, non-essential amino acids, pyruvate, beta-mercaptoethanol, knockout replacement serum) for

7 days. Half-media changes were performed daily. On day 7 spheroids were transferred to cortical maturation media (DMEM/F12, Glutamax, N2, penicillin-streptomycin) in a plastic culture dish for 3 days.

Tissue preparation

Embryonic cortices were dissected and fixed in 4% paraformaldehyde in PBS overnight. Tissues were cryosectioned (10–50 μ m sections) and processed for immunohistochemistry, in situ hybridization, or RNAScope fluorescent in situ hybridization. For immunohistochemistry, spheroids were fixed in 4% paraformaldehyde for 30 min on ice. After three washes in PBS, Spheroids were transferred to 30% sucrose for approximately 2 h on ice (until spheroids sink). Spheroids were cryosectioned at 8–10 μ m.

RNA sample collection

E12.5 lateral cortex samples were lysed in QIAzol reagent, and RNA was extracted following the manufacturer's instructions (miRNeasy Micro Kit, Qiagen). Six samples were used for RNA sequencing: four control females and two Foxp1^{ckO} females. RNA concentration and integrity were assessed with Agilent RNA ScreenTape analysis using the Agilent 2100 Bioanalyzer. All samples used in downstream analyses had a RIN > 9.7. Spheroids were lysed in Qiazol reagent and RNA was extracted following manufacturer's instructions (RNAeasy Micro Kit, Qiagen).

RNA sequencing and analysis

RNA samples were sent to the UCLA Neuroscience Genomics Core for library preparation and sequencing. Sample libraries were generated using TruSeq Stranded RNA kit and sequenced with paired-end 150 base pair reads on two lanes using the Illumina HiSeq 3000. Each sample contained 58–91 million reads (an average of 79 million). All samples of raw sequence data passed quality control using FastQC (Andrews, 2010). The data was mapped to the mouse MM10 genome (Gencode version 17) using STAR aligner (Dobin et al, 2013) with default parameters. MultiQC was used to aggregate quality metrics produced by STAR (Ewels et al, 2016). Within each sample, 92–93% of reads were uniquely mapped and used for further analyses. BAM files produced by STAR were sorted and converted to SAM files using samtools (Li et al, 2009). Gene read counts were estimated using HTSeq union gene counts (Anders et al, 2015). Sequencing bias was estimated using Picard Tools (broadinstitute.github.io/picard/) functions CollectRnaSeqMetrics, CollectGcBiasMetrics, CollectAlignmentSummaryMetrics, and CollectInsertSizeMetrics. An ANOVA was used to determine if these metrics were having a significant effect on the data. Genes with expression (< 10 counts) across half the samples were excluded, leaving 17,068 genes that passed the filter for further analyses. Principle component analysis was performed in R using the function "prcomp" on data normalized by variance stabilizing transformation (VST). Differential gene expression analysis was performed using DESeq2 (Love et al, 2014) with the model ~Group + Litter. False discovery rate (FDR) < 5% was used as a cutoff to determine if genes were differentially expressed. Gene ontology and pathway analysis were performed using gprofiler2 (<https://biit.cs.ut.ee/gprofiler/gost>) and disgenet (<https://www.disgenet.org/>). This work used computational and storage services associated with the Hoffman2

Shared Cluster provided by UCLA Institute for Digital Research and Education's Research Technology Group. All data and code used in analyses will be shared publicly on GEO and github.

Quantitative PCR

Reverse Transcriptase quantitative PCR (RT-qPCR) was performed using the SuperScript VILO First-Strand Synthesis System (Invitrogen). For each sample, >500 ng of total RNA was used for cDNA synthesis. In each qPCR reaction, 1–4 ng cDNA was combined with PowerTrack SYBR Green Master Mix (ThermoFisher) and primer pairs. All primer pairs were validated for ≥ 1.8 amplification efficiency. Samples were run on a ThermoFisher QuantStudio 5 real-time PCR system in triplicate, and log₂ fold change was determined by normalizing the delta-delta CT to the internal reference gene Beta Actin. Primers were designed using Primer3-plus. Primer sets used; *Slc2a1* F: *acttgctctcttggccaagc* R: *aaagcctcttagctcagagttc*; *Ldha* F: *aactgcaggcttcgattacc* R: *tgcatcatggacgtacacac*; *Vegfa* F: *acacgacaaaccattcctg* R: *tccacaaagcatgcatgctc*; *Aldoa* F: *ctgaataggctgcttctcttg* R: *aaggactaaggagcgaacgc*; *Pdk1* F: *atgctggctggtttgatgc* R: *ttcagtcaccccgaatgc*; *Pfkl* F: *ggacaaaccgggtacacagg* R: *atccgcagtttccaggtc*; *Pfkl* F: *gcatccctgagctttgaacag* R: *aatgtgctttgctggagtc*; *Slc16a4* F: *tggtgtttccaccaagcag* R: *taggctacatgcccagatcac*; *Actb* F: *tttgccgttttgactcagg* R: *actttgggggatgtttgctc*.

Western blot analysis

Whole-cell extracts from mESCs cultured in feeder-free 2i media were prepared in a modified RIPA lysis buffer: 50 mM Tris (pH 7.4), 150 mM NaCl, 1% NP-40, 0.25% sodium deoxycholate, and 1x SigmaFast protease inhibitor cocktail. Spheroids were lysed in RIPA buffer and protease inhibitors. Protein concentration was determined with a BCA kit (Thermo Fisher Scientific) and normalized to 1.0–2.0 µg/µl. 20–25 µl of protein was mixed with sample buffer and 50–100 mM DTT. Protein was transferred to a PVDF membrane, blocked with either 1% BSA or Intercept (TBS) Blocking Solution (LI-COR), and blotted with primary antibodies at 4 °C overnight. Primary antibodies used: Foxp1 (1:1000, D35D10, #4402, Cell Signaling) (Glut1 (2 µg/ml, #sc-377228, Santa Cruz Biotechnology), HIF-1α (1 µg/ml, #AF1935, R&D Systems), Ldha (1:1000, #2012 Cell Signaling), Vegfa (1:500, #19003, Proteintech), Beta-Actin (1 µg/ml, 664802, Biologend), Gapdh (1:1000, #926-422116, LI-COR), α-Tubulin (Synaptic Systems, 1:2000, #302 204). Western blots were imaged on an Odyssey DLx Imager system.

RNA probe synthesis and in situ hybridization

Riboprobes were generated using primers designed against the 5' or 3' UTRs of mouse *Aldoa*, *Ldha*, *Slc16a4*, *Pfkl*, *Pfkl*, *Pfkl*, *Pdk1*, and *Slc2a1* transcripts. In situ hybridization was performed on sections as previously described (Pearson et al, 2011). Primer sets used: *Aldoa* F: *cactgggctcactttctgt* R: *aaggatggcagatttagca*; *Ldha* F: *gcttctagcagaccacac* R: *gacacttgggtggtggtc*; *Slc16a4* F: *gaggtccagagactggcaac* R: *tgtcccttagcagagatgg*; *Pfkl* F: *gcatcaccaactgtgtgtc* R: *tgatgatgttcagccagag*; *Pdk1* F: *tctctgcagctaccta* R: *gcacctgtctgagcttc*; *Slc2a1* F: *agcagtgaagtccaggagga* R: *ctggctcaggcaaggaaag*; *Pfkl* F: *cccagcttctgttagag* R: *agaggatgaggcaagtc*.

RNAScope fluorescent in situ hybridization

RNAScope (acdbio) FISH was performed on cryosections per manufacturer guidelines. Probes used were Vegfa #412261-C3 and Foxp1#485221.

Immunohistochemistry

Immunohistochemistry was performed on tissue sections as previously described (Pearson et al, 2020). In brief, slides were post-fixed for 10 min in 4% PFA (post-fix was not included when performing IHC on spheroids). After three PBST (0.1% Triton-X) washes and 10 min in antibody block, primary antibodies were applied overnight. Primary antibodies were used at the following dilutions: Foxp1 1:16,000 (Rouso et al, 2012), Glut1 1:100 (Abcam ab128033), Ldha 1:250 Abcam ab52488, HIF-1α (1:100 R&D Systems AF1935), TUJ1 1:1000 (BioLegend 801201), Vegfa 1:250 (Proteintech 19003-1-AP), Tbr2 1:500 (Millipore Sigma AB15894), CD31 1:100 (R&D Systems AF3628), Nestin 1:1000 (Novus NB100-1604), Tbr1 1:1000 (Abcam ab31940), Ctip2 1:1000 (Abcam ab18465), Pax6 1:1000 (MBL PD022). Donkey secondary antibodies (Jackson Immunoresearch) and DAPI (1mg/ml) were used at 1:1000. 2 µM of Isolectin GS-IB4 from *Griffonia simplicifolia* conjugated to Alexa Fluor 647 (ThermoFisher Cat.I32450) was diluted with secondary antibodies and incubated on slides for 1 h at room temperature. When expression levels were to be measured, coverslips were applied to ensure even distribution across the slide.

Image acquisition

Confocal images were acquired using Zeiss LSM 780, LSM 800, and Olympus FV1000 laser scanning confocal microscopes and processed with Zen Blue and Fluoview software. DIC images of in situ hybridizations were collected using a Zeiss Axioimager microscope and Axiovision software.

Quantification and statistical analysis

N numbers and statistical analyses for each figure are in each figure legend. Images were processed and compiled using Adobe Photoshop with adjustments applied to the entire image and restricted to brightness, contrast, and levels. Images shown in figures as comparisons, e.g., intensity levels, were obtained and processed in parallel using identical settings. Composite images were assembled using Adobe Illustrator software.

For each experiment, the mean gray values (relative to background) of labeled Nestin⁺ RG per section were quantified from 3–6 sections per embryo (sampled at ~100 µm intervals along the rostrocaudal axis within the presumptive somatosensory cortex). Each mutant's mean gray value of staining was normalized to littermate controls. Mean gray values were measured using Fiji software, with background staining levels subtracted. For vessel measurements, contiguous IB4⁺ vessels in 50-µm-thick sections were identified using surface rendering software in Imaris (minimum threshold 742, minimum number of voxels 1.7×10^4). Measurements for each PVP vessel were recorded (PNVP vasculature was not included). In Fig. 3A,B, each hemisphere was divided into three identically sized dorsal-ventral bins, and vessels

within each bin were quantified. Vessel length, volume, and branch points were analyzed using Imaris imaging software.

gprolifer and disgenet online database tools were used to analyze differentially expressed RNA Sequencing gene lists. Imaris was used to analyze blood vessel length and branching; surface-rendered images were generated to identify and measure individual vessels. GraphPad Prism software was used to determine the normality of each dataset (using the Shapiro–Wilk test and Kolmogorov–Smirnov Normality tests), and the appropriate parametric test was applied. Student's t-tests and Mann–Whitney tests were calculated using Prism software. Significance was assumed when $p < 0.05$. The results of statistical tests (p values and sample sizes) are reported in Figure legends. All data are presented as mean \pm SEM. Sample size estimates were not used. Spheroid data sets were blinded. Embryonic cortex data sets were not blinded.

Data availability

RNA-seq data have been deposited at NCBI Gene Expression Omnibus, GEO accession number [GSE217364](https://doi.org/10.1101/202302193) are publicly available as of the publication date. No original code was created. Any additional information required to reanalyze the data reported in this paper is available from the lead contact upon request. Further information and requests for resources and reagents should be directed to the Lead Contact, Caroline Alayne Pearson (cap4010@med.cornell.edu).

Expanded view data, supplementary information, appendices are available for this paper at <https://doi.org/10.1038/s44319-024-00131-8>.

Peer review information

A peer review file is available at <https://doi.org/10.1038/s44319-024-00131-8>

References

- Anders S, Pyl PT, Huber W (2015) HTSeq—a Python framework to work with high-throughput sequencing data. *Bioinformatics* 31(2):166–169
- Andrews MG, Pearson CA (2024) Toward an understanding of glucose metabolism in radial glial biology and brain development. *Life Sci Alliance* 7. <https://doi.org/10.26508/lsa.202302193>
- Andrews S (2010) FastQC: a quality control tool for high throughput sequence data. Preprint at <http://www.bioinformatics.babraham.ac.uk/projects/fastqc>
- Azmitia EC, Saccomano ZT, Alzoobae MF, Boldrini M, Whitaker-Azmitia PM (2016) Persistent angiogenesis in the autism brain: an immunocytochemical study of postmortem cortex, brainstem and cerebellum. *J Autism Dev Disord* 46(4):1307–1318
- Bagnall J, Leedale J, Taylor SE, Spiller DG, White MRH, Sharkey KJ, Bearon RN, Sée V (2014) Tight control of hypoxia-inducible factor- α transient dynamics is essential for cell survival in hypoxia. *J Biol Chem* 289(9):5549–5564
- Baruah J, Vasudevan A (2019) The vessels shaping mental health or illness. *Open Neurol J* 13. <https://doi.org/10.2174/1874205X01913010001>
- Beattie R, Hippenmeyer S (2017) Mechanisms of radial glia progenitor cell lineage progression. *FEBS Lett* 591(24):3993–4008
- Brocato J, Chervona Y, Costa M (2014) Molecular responses to hypoxia-inducible factor 1 α and beyond. *Mol Pharmacol* 85(5):651–657
- Corrado C, Fontana S (2020) Hypoxia and HIF signaling: one axis with divergent effects. *Int J Mol Sci* 21(16). <https://doi.org/10.3390/ijms21165611>
- Cunningham CL, Martínez-Cerdeño V, Noctor SC (2013) Microglia regulate the number of neural precursor cells in the developing cerebral cortex. *J Neurosci* 33(10):4216–4233
- Daneman R, Agalliu D, Zhou L, Kuhnert F, Kuo CJ, Barres BA (2009) Wnt/ β -catenin signaling is required for CNS, but not non-CNS, angiogenesis. *Proc Natl Acad Sci USA* 106(2):641–646
- Desai AR, McConnell SK (2000) Progressive restriction in fate potential by neural progenitors during cerebral cortical development. *Development* 127(13):2863–2872
- Dobin A, Davis CA, Schlesinger F, Drenkow J, Zaleski C, Jha S, Batut P, Chaisson M, Gingeras TR (2013) STAR: ultrafast universal RNA-seq aligner. *Bioinformatics* 29(1):15–21
- Dong X, Zhang Q, Yu X, Wang D, Ma J, Ma J, Shi S-H (2022) Metabolic lactate production coordinates vasculature development and progenitor behavior in the developing mouse neocortex. *Nat Neurosci* 25(7):865–875
- Eiraku M, Sasai Y (2011) Mouse embryonic stem cell culture for generation of three-dimensional retinal and cortical tissues. *Nat Protoc* 7(1):69–79
- Ewels P, Magnusson M, Lundin S, Käller M (2016) MultiQC: summarize analysis results for multiple tools and samples in a single report. *Bioinformatics* 32(19):3047–3048
- Feng X, Ippolito GC, Tian L, Wiehagen K, Oh S, Sambandam A, Willen J, Bunte RM, Maika SD, Harriss JV et al (2010) Foxp1 is an essential transcriptional regulator for the generation of quiescent naive T cells during thymocyte development. *Blood* 115(3):510–518
- Frost J, Galdeano C, Soares P, Gadd MS, Grzes KM, Ellis L, Epemolu O, Shimamura S, Bantscheff M, Grandi P et al (2016) Potent and selective chemical probe of hypoxic signalling downstream of HIF- α hydroxylation via VHL inhibition. *Nat Commun* 7:13312
- Gerhardt H, Golding M, Fruttiger M, Ruhrberg C, Lundkvist A, Abramsson A, Jeltsch M, Mitchell C, Alitalo K, Shima D et al (2003) VEGF guides angiogenic sprouting utilizing endothelial tip cell filopodia. *J Cell Biol* 161(6):1163–1177
- Gomez GG, Volinia S, Croce CM, Zanca C, Li M, Emmett R, Gutmann DH, Brennan CW, Furnari FB, Cavenee WK (2014) Suppression of microRNA-9 by mutant EGFR signaling upregulates FOXP1 to enhance glioblastoma tumorigenicity. *Cancer Res* 74(5):1429–1439
- Grundmann S, Lindmayer C, Hans FP, Hoefler I, Helbing T, Pasterkamp G, Bode C, de Kleijn D, Moser M (2013) FoxP1 stimulates angiogenesis by repressing the inhibitory guidance protein semaphorin 5B in endothelial cells. *PLoS ONE* 8(9):e70873
- Haigh JJ, Morelli PI, Gerhardt H, Haigh K, Tsien J, Damert A, Miquerol L, Muhlner U, Klein R, Ferrara N et al (2003) Cortical and retinal defects caused by dosage-dependent reductions in VEGF-A paracrine signaling. *Dev Biol* 262(2):225–241
- Hubbi ME, Gilkes DM, Hu H, Kshitiz, Ahmed I, Semenza GL (2014) Cyclin-dependent kinases regulate lysosomal degradation of hypoxia-inducible factor 1 α to promote cell-cycle progression. *Proc Natl Acad Sci USA* 111(32):E3325–34
- Iwasato T, Nomura R, Ando R, Ikeda T, Tanaka M, Itohara S (2004) Dorsal telencephalon-specific expression of Cre recombinase in PAC transgenic mice. *Genesis* 38(3):130–138
- Ji S, Zhou W, Li X, Liu S, Wang F, Li X, Zhao T, Ji G, Du J, Hao A (2019) Maternal hyperglycemia disturbs neocortical neurogenesis via epigenetic regulation in C57BL/6J mice. *Cell Death Dis* 10(3):211

- Jiang J, Hu Y, Zhang B, Shi Y, Zhang J, Wu X, Yao P (2017) MicroRNA-9 regulates mammalian axon regeneration in peripheral nerve injury. *Mol Pain* 13:1744806917711612
- Komabayashi-Suzuki M, Yamanishi E, Watanabe C, Okamura M, Tabata H, Iwai R, Ajioka I, Matsushita J, Kidoya H, Takakura N et al (2019) Spatiotemporally dependent vascularization is differently utilized among neural progenitor subtypes during neocortical development. *Cell Rep* 29(5):1113–1129.e5
- Lange C, Turrero Garcia M, Decimo I, Bifari F, Eelen G, Quaegebeur A, Boon R, Zhao H, Boeckx B, Chang J et al (2016) Relief of hypoxia by angiogenesis promotes neural stem cell differentiation by targeting glycolysis. *EMBO J* 35(9):924–941
- Lee SH, Bae SC, Kim KW, Lee YM (2014) RUNX3 inhibits hypoxia-inducible factor-1 α protein stability by interacting with prolyl hydroxylases in gastric cancer cells. *Oncogene* 33(11):1458–1467
- Lee S-H, Che X, Jeong J-H, Choi J-Y, Lee Y-J, Lee Y-H, Bae S-C, Lee Y-M (2012) Runx2 protein stabilizes hypoxia-inducible factor-1 α through competition with von Hippel-Lindau protein (pVHL) and stimulates angiogenesis in growth plate hypertrophic chondrocytes. *J Biol Chem* 287(18):14760–14771
- Li C, Zhang K, Chen J, Chen L, Wang R, Chu X (2017) MicroRNAs as regulators and mediators of forkhead box transcription factors function in human cancers. *Oncotarget* 8(7):12433–12450
- Li H, Handsaker B, Wysoker A, Fennell T, Ruan J, Homer N, Marth G, Abecasis G, Durbin R (2009) The sequence alignment/Map format and SAMtools. *Bioinformatics* 25(16):2078–2079
- Love MI, Huber W, Anders S (2014) Moderated estimation of fold change and dispersion for RNA-seq data with DESeq2. *Genome Biol* 15(12):550
- Madelaine R, Sloan SA, Huber N, Notwell JH, Leung LC, Skariah G, Halluin C, Paşca SP, Bejerano G, Krasnow et al (2017) MicroRNA-9 couples brain neurogenesis and angiogenesis. *Cell Rep* 20(7):1533–1542
- Nguyen LK, Cavadas MAS, Scholz CC, Fitzpatrick SF, Bruning U, Cummins EP, Tambuwala MM, Manresa MC, Kholodenko BN, Taylor CT et al (2013) A dynamic model of the hypoxia-inducible factor 1 α (HIF-1 α) network. *J Cell Sci* 126(Pt 6):1454–1463
- Otaegi G, Pollock A, Hong J, Sun T (2011) MicroRNA miR-9 modifies motor neuron columns by a tuning regulation of FoxP1 levels in developing spinal cords. *J Neurosci* 31(3):809–818
- Ouellette J, Lacoste B (2021) From neurodevelopmental to neurodegenerative disorders: the vascular continuum. *Front Aging Neurosci* 13:749026
- Pearson CA, Moore DM, Tucker HO, Dekker JD, Hu H, Miquelajáuregui A, Novitch BG (2020) Foxp1 regulates neural stem cell self-renewal and bias toward deep layer cortical fates. *Cell Rep* 30(6):1964–1981.e3
- Pearson CA, Ohyama K, Manning L, Aghamohammadzadeh S, Sang H, Placzek M (2011) FGF-dependent midline-derived progenitor cells in hypothalamic infundibular development. *Development* 138(12):2613–2624
- Peng ZG, Zhou MY, Huang Y, Qiu JH, Wang LS, Liao SH, Dong S, Chen GQ (2008) Physical and functional interaction of Runt-related protein 1 with hypoxia-inducible factor-1 α . *Oncogene* 27(6):839–847
- Penna E, Mangum JM, Shepherd H, Martínez-Cerdeño V, Noctor SC (2021) Development of the neuro-immune-vascular plexus in the ventricular zone of the prenatal rat neocortex. *Cereb Cortex* 31(4):2139–2155
- Radhakrishnan B, Alwin Prem Anand A (2016) Role of miRNA-9 in brain development. *J Exp Neurosci* 10:101–120
- Rouso DL, Pearson CA, Gaber ZB, Miquelajáuregui A, Li S, Portera-Cailliau C, Morrisey EE, Novitch BG (2012) Foxp-mediated suppression of N-cadherin regulates neuroepithelial character and progenitor maintenance in the CNS. *Neuron* 74(2):314–330
- Sengupta T, Abraham G, Xu Y, Clurman BE, Minella AC (2011) Hypoxia-inducible factor 1 is activated by dysregulated cyclin E during mammary epithelial morphogenesis. *Mol Cell Biol* 31(18):3885–3895
- Shen Q, Wang Y, Dimos JT, Fasano CA, Phoenix TN, Lemischka IR, Ivanova NB, Stifani S, Morrisey EE, Temple S (2006) The timing of cortical neurogenesis is encoded within lineages of individual progenitor cells. *Nat Neurosci* 9(6):743–751
- Taverna E, Götz M, Huttner WB (2014) The cell biology of neurogenesis: toward an understanding of the development and evolution of the neocortex. *Ann Rev Cell Dev Biol* 30:465–502
- Telley L, Agirman G, Prados J, Amberg N, Fièvre S, Oberst P, Bartolini G, Vitali I, Cadilhac C, Hippenmeyer et al (2019) Temporal patterning of apical progenitors and their daughter neurons in the developing neocortex. *Science* 364(6440):eaav2522
- Vasudevan A, Long JE, Crandall JE, Rubenstein JLR, Bhide PG (2008) Compartment-specific transcription factors orchestrate angiogenesis gradients in the embryonic brain. *Nat Neurosci* 11(4):429–439
- Zhang J, Roberts JM, Chang F, Schwakopf J, Vetter ML (2023) Jarid2 promotes temporal progression of retinal progenitors via repression of Foxp1. *Cell Rep* 42(3):112237
- Zhang Y, Li S, Yuan L, Tian Y, Weidenfeld J, Yang J, Liu F, Chokas AL, Morrisey EE (2010) Foxp1 coordinates cardiomyocyte proliferation through both cell-autonomous and nonautonomous mechanisms. *Genes Dev* 24(16):1746–1757

Acknowledgements

We are grateful to H. Tucker and the RIKEN BioResource Center for mouse strains used in this study. We appreciate K. Phan, A. Schlusche, and S. Singh for technical assistance, the UCLA Broad Stem Cell Research Center (BSCRC) and the Center for Neurogenetics at WCM for microscopy and other resources, and the UCLA Sequencing Core for technical assistance. We thank Novitch and Ross lab members for their valuable input and discussions, and M. Placzek, M.G Andrews, C. Iadecola, and S.J Butler for critical input on the manuscript. JEB was supported by the UCLA BSCRC Rose Hills Foundation Graduate Scholarship Training Program (EDUC4-12753). LG, TM, and JHK were supported by the NIH R00GM132518 and the NIH/NCI Cancer Center Support Grant P30CA015704. MRH was supported by R01NS126209 and the American Heart Association Career Development Award (AHA941434). NIH R01NS105477 supported MER. The UCLA Broad Stem Cell Research Center and the NIH R01NS089817 supported BGN. CAP was supported by research awards from the UCLA-California Institute for Regenerative Medicine Training Grant (TG2-01169), the Brain and Spine Institute at New York Presbyterian Hospital and Weill Cornell Medicine, the GLUT1-Deficiency Foundation and the American Epilepsy Society Junior Investigator award. We also acknowledge the support of the NINDS-sponsored UCLA Informatics Center for Neurogenetics and Neurogenomics (P30NS062691) and the UCLA Intellectual and Developmental Disabilities Research Center Genetics and Genomics Core supported by the NICHD (U54HD087101 and P50HD103557).

Author contributions

Jessie E Buth: Formal analysis; Investigation; Methodology; Writing—original draft. **Catherine E Dyeovich:** Formal analysis; Investigation; Methodology; Writing—original draft; Writing—review and editing. **Alexandra Rubin:** Formal analysis; Investigation; Methodology; Writing—review and editing. **Chengbing Wang:** Investigation; Methodology. **Lei Gao:** Investigation; Methodology. **Tessa Marks:** Investigation; Methodology. **Michael RM Harrison:** Conceptualization; Formal analysis; Investigation; Methodology. **Jennifer H Kong:** Resources; Funding acquisition; Investigation; Methodology. **M Elizabeth Ross:** Resources; Funding acquisition; Investigation; Methodology; Writing—original draft; Writing—review and editing. **Bennett G Novitch:** Conceptualization; Resources; Funding acquisition; Methodology; Writing—original draft; Project administration; Writing—review and editing. **Caroline Alayne Pearson:** Conceptualization; Resources; Data curation; Formal analysis; Supervision;

Funding acquisition; Validation; Investigation; Visualization; Methodology; Writing—original draft; Project administration; Writing—review and editing.

Disclosure and competing interests statement

The authors declare no competing interests.

Open Access This article is licensed under a Creative Commons Attribution 4.0 International License, which permits use, sharing, adaptation, distribution and reproduction in any medium or format, as long as you give appropriate credit to the original author(s) and the source, provide a link to the Creative Commons licence, and indicate if changes were made. The images or other third party material in this article are included in the article's Creative Commons licence, unless indicated otherwise in a credit line to the material. If material is not

included in the article's Creative Commons licence and your intended use is not permitted by statutory regulation or exceeds the permitted use, you will need to obtain permission directly from the copyright holder. To view a copy of this licence, visit <http://creativecommons.org/licenses/by/4.0/>. Creative Commons Public Domain Dedication waiver <http://creativecommons.org/public-domain/zero/1.0/> applies to the data associated with this article, unless otherwise stated in a credit line to the data, but does not extend to the graphical or creative elements of illustrations, charts, or figures. This waiver removes legal barriers to the re-use and mining of research data. According to standard scholarly practice, it is recommended to provide appropriate citation and attribution whenever technically possible.

© The Author(s) 2024

Expanded View Figures

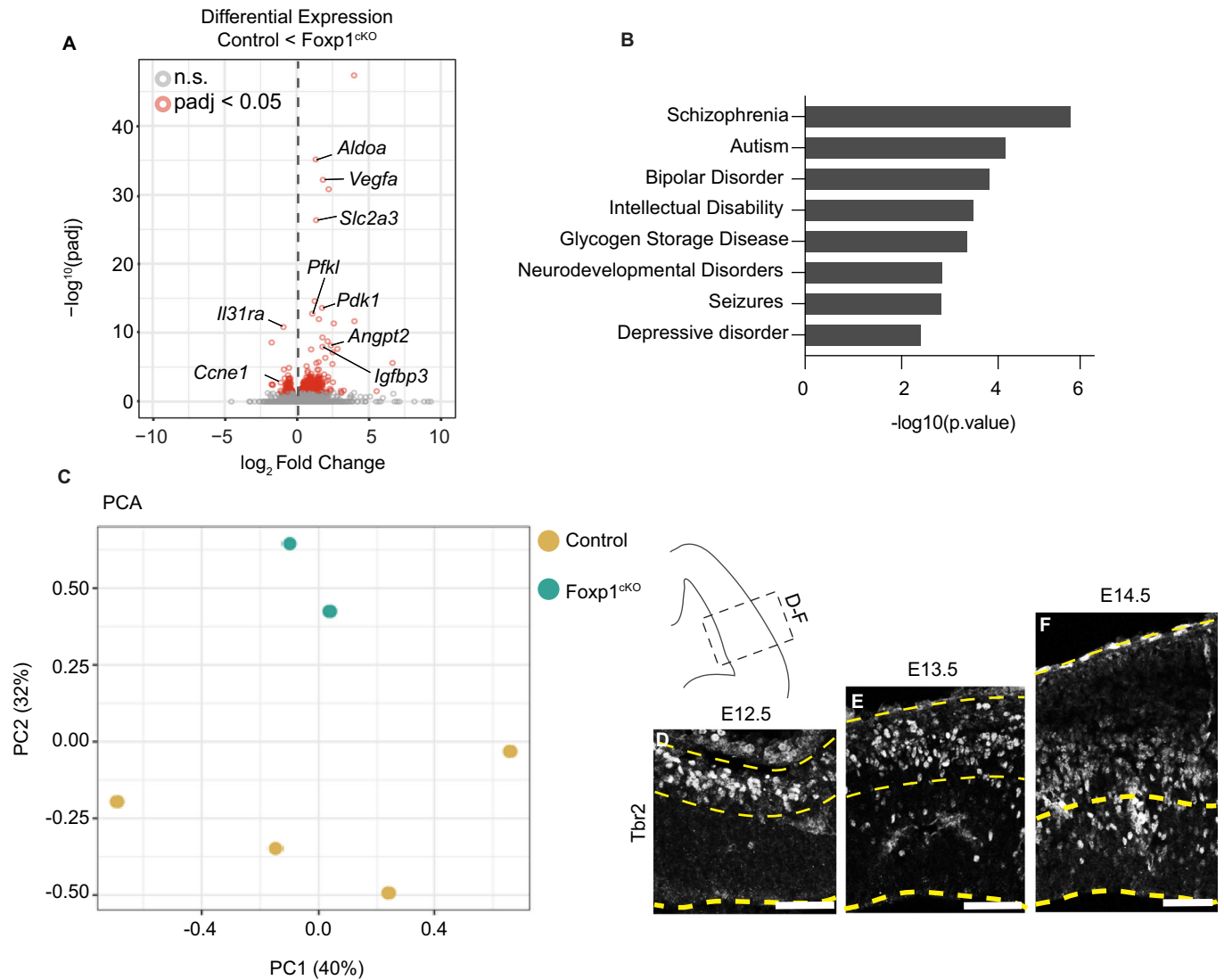
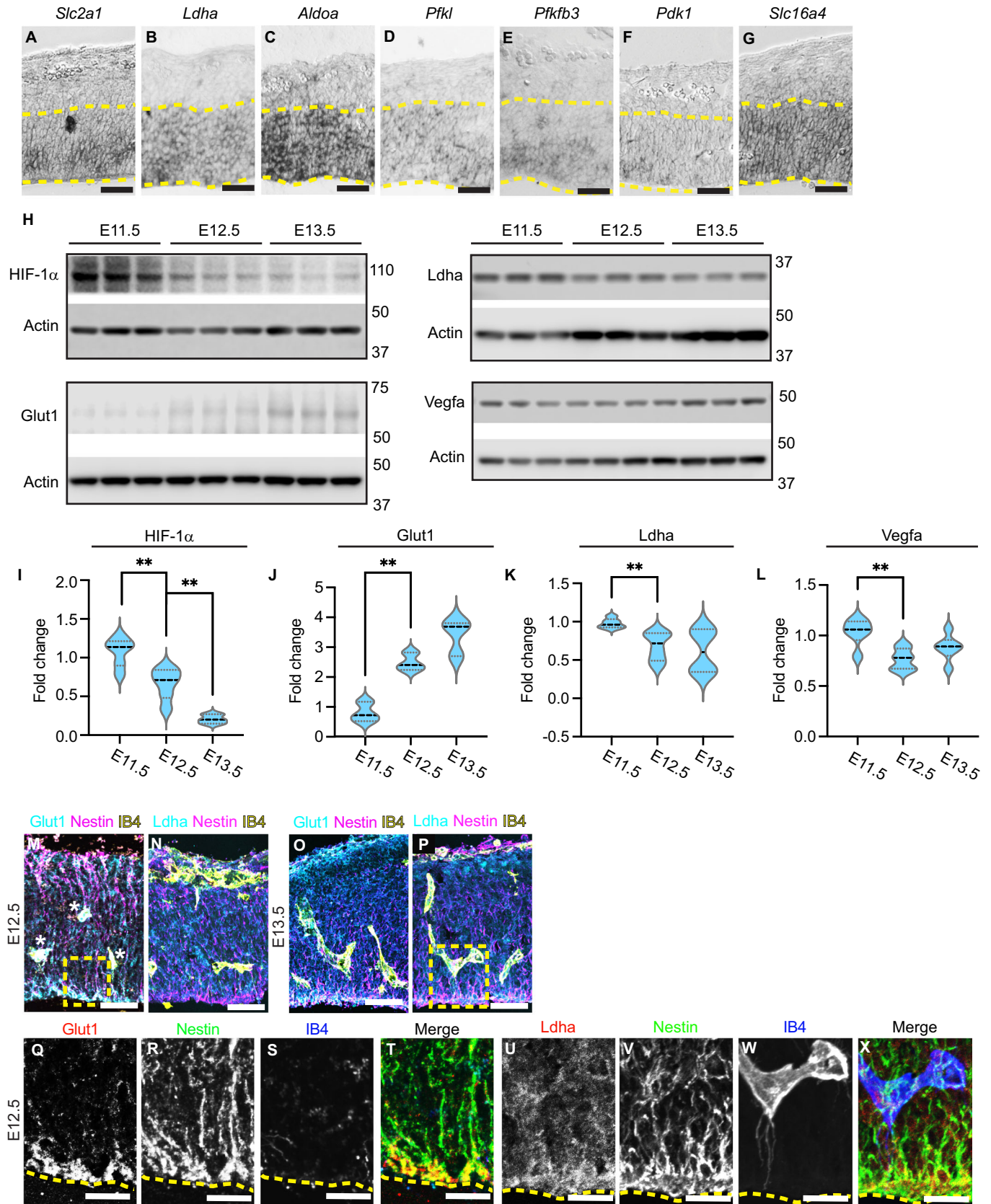


Figure EV1. RNA Seq analysis of Foxp1^{CKO} cortex.

(A) Volcano plot of gene expression changes in the absence of Foxp1 in E12.5 lateral cortex compared to control embryos. Gray circles denote non-significant gene changes (adjusted p -value > 0.05); red circles denote significantly differentially expressed genes (adjusted p -value < 0.05). (B) Human disorders associated with genes significantly misregulated in Foxp1^{CKO} mutants at E12.5. (C) The principal component analysis (PCA) of control and Foxp1^{CKO} mutants shows PC1 and PC2. (D-F) IHC for Tbr2⁺ intermediate progenitors in wild-type cortex at E12.5, E13.5, and E14.5. Schematic denotes area image in (D-F). Scale bars 50 μm . Data information: significance determined by ANOVA (A, B).



◀ Figure EV2. HIF-1 α target gene expression in RG in the wild-type cortex.

(A–G) Wild-type mRNA expression of glycolysis genes *Slc2a1*, *Ldha*, *Aldoa*, *Pfkfb3*, *Pdk1*, and *Slc16a4* in the wild-type lateral cortex at E12.5. (H) Western blot analysis of HIF-1 α , Glut1, *Ldha*, and *Vegfa* (with Beta Actin) in wild-type cortical lysates at E11.5, E12.5, E13.5. (I) Fold change of HIF-1 α levels normalized to Beta Actin between E11.5 and E13.5. (J) Fold change of Glut1 levels normalized to Beta Actin between E11.5 and E13.5. (K) Fold change of *Ldha* levels normalized to Beta Actin between E11.5 and E13.5. (L) Fold change of *Vegfa* levels normalized to Actin between E11.5 and E13.5. (M, N) IHC for Glut1 and *Ldha* with Isolectin B4, and Nestin at E12.5 in the wild-type cortex. (O, P) IHC for Glut1 or *Ldha* with Isolectin B4, and Nestin at E13.5 in the wild-type cortex. Boxed areas are magnified in (Q–X). (Q–T) High magnification image of IHC for Glut1 in Nestin+ RG at E12.5. Isolectin B4 labels blood vessels. (U–X) High magnification images of IHC for *Ldha* in Nestin+ RG at E13.5. Isolectin B4 labels blood vessels. Scale bars 50 μ m (A–K), 10 μ m (L–S). Data information: $N = 5$ –9 embryos per time point, 3–6 replicates. $p = 0.0039$ and 0.0073 (I). $N = 5$ –9 embryos per time point, 3 replicates. $p = 0.0028$ (J). $N = 5$ –9 embryos per time point, 6 replicates. $p = 0.0041$ (K). $N = 5$ –9 embryos per time point, 6 replicates. $p = 0.0017$ (L). All Student's t-tests. All data represented as mean \pm SEM. Source data are available online for this figure.

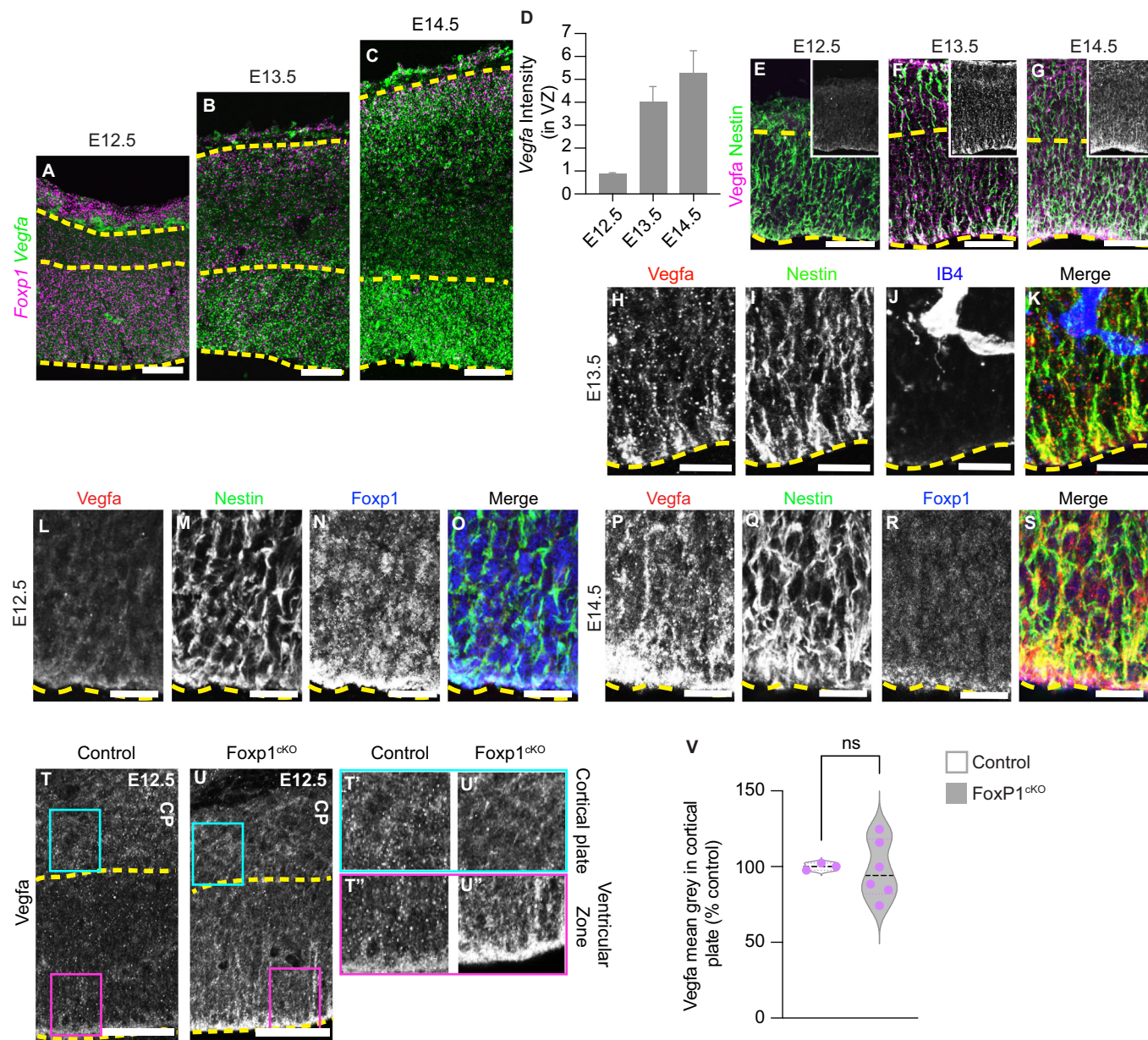


Figure EV3. Spatial and temporal relationship between Foxp1 and Vegfa in radial glia and neurons.

(A-C) RNA Scope analysis of Vegfa and Foxp1 in the wild-type cortex at E12.5-E14.5. (D) Vegfa mean gray value (over background) in the ventricular zone between E12.5-E14.5. (E-G) IHC for Vegfa and Nestin in the wild-type cortex at E12.5, E13.5, and E14.5. (H-K) High magnification images of Vegfa, Nestin, and IB4 at the apical surface of the VZ at E13.5. (L-S) High magnification images of IHC for Vegfa, Nestin, and Foxp1 at E12.5 and E14.5 in wild-type cortex. (T-U) IHC for Vegfa in the cortex at E12.5 in control and Foxp1^{ckO} embryos. Cyan boxes represent areas in CP magnified in T' and U'. Magenta boxes represent the area within VZ magnified in T'' and U''.

(V) Quantification of Vegfa mean gray values in the cortical plate in control and Foxp1^{ckO} cortex at E12.5. Scale bars 50 μm (A-G, T, U) 10 μm (H-S). Data information: N = 5-7 embryos per time point (D). N = 3 control, 6 mutant (2 litters). $p = 0.8674$, Student's t-test (V). All data represented as mean ± SEM.

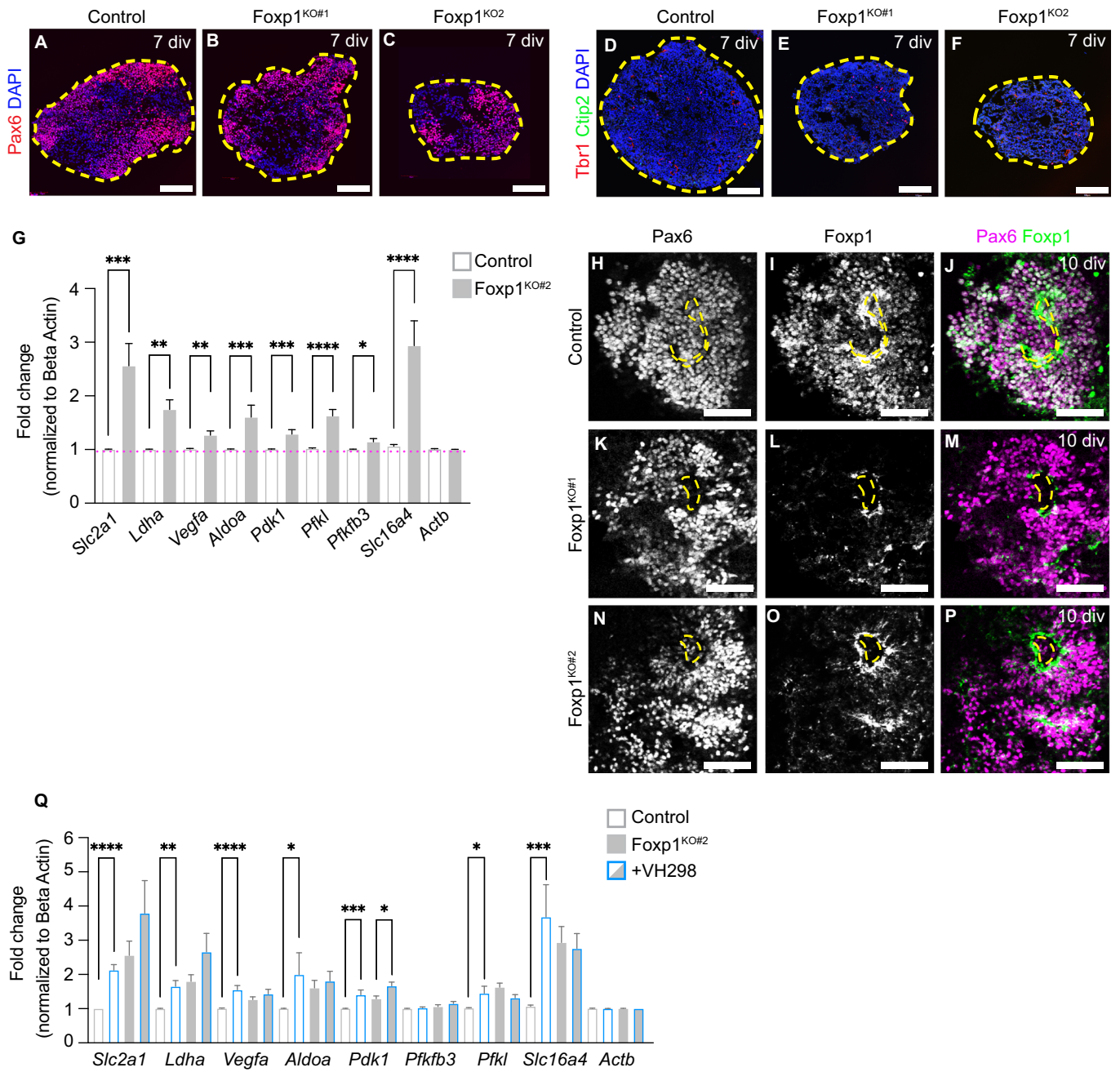


Figure EV4. Analysis of Foxp1-deficient cortical spheroids.

(A-C) IHC for Pax6 in control and Foxp1^{KO} spheroids at 7 days in vitro (div). (D-F) IHC for Ctip2 and Tbr1⁺ neurons in control and Foxp1^{KO} spheroids at 7 div. (G) qPCR analysis of HIF-1α target gene expression in control and Foxp1^{KO#2} spheroids at 10 div. (H-P) IHC for Foxp1 in Pax6⁺ NPCs in control and Foxp1^{KO} spheroids at 10 div. (Q) qPCR analysis of HIF-1α target gene expression in control and Foxp1^{KO#2} spheroids at 10 div. treated with DMSO or VH298. Scale bars 100 μm (A-F), 50 μm (H-P). Data information: N = 10–12 spheroids from 3 individual batches. p = 0.0007 (*Slc2a1*), 0.0108 (*Ldha*), 0.0031 (*Vegfa*), 0.0009 (*Aldoa*), 0.0002 (*Pdk1*), 0.0002 (*Pfkf*), 0.0226 (*Pfkfb3*), <0.0001 (*Slc16a4*). Student's t-test (G). p = <0.0001 (*Slc2a1*, control), 0.0013 (*Ldha*, control) <0.0001 (*Vegfa*, control), 0.0179 (*Aldoa*, control) 0.0002 (*Pdk1*, control), 0.0312 (*Pdk1*, Foxp1^{KO#2}), 0.0201 (*Pfkf*, control), 0.0003 (*Slc16a4*, control). Student's t-test (Q). All data represented as mean ± SEM.